5
Validation tests

The implementation described previously is validated in this chapter. This is achieved by comparing the results of the XFEMHF code with analytical or other software solutions. First, the results of a single propagating planar fracture are compared with the analytical solution of the near-K vertex of the KGD model.

Next, a group of simulations focus in flow through fractured media. A problem with unidimensional flow in a fractured element is compared with the analytical solution. Plus, bi-dimensional flow both in permanent and transient regimes is tested in three examples and compared with models with interface elements. In all models of this section a variation of hydraulic parameters is applied, in order to validate different percolation behaviours.

Finally, the validation of the contact model with friction is achieved, first by using a one-element mesh with a single fracture followed by a multi-fractured problem. The single element models are used for three different situations where fracture position or load conditions change. First, an element with a horizontal fracture is subjected to a vertical cyclic displacement applied at its top. Second, an element with a horizontal fracture is subjected to a horizontal monotonic displacement at its top for three different vertical confining stresses. Third, an element with an inclined fracture is subjected to a vertical cyclic displacement applied at its top. In the multi-fractured model an unconfined compression test is simulated and the stress trajectories of the fractures are plotted against the implemented Mohr-Coulomb failure surface.

5.1.
KGD analytical solution

General description of the simulation

As stated in Chapter 2, there are analytical formulations for propagating fractures in a homogeneous medium. The KGD solution assumes a fracture which is infinite in one of its dimensions, so this means it can be modelled using a two-dimensional plane strain model. In this simulation, a numerical model is compared with the KGD K-vertex analytical storage-toughness solution, as presented by Bunger, Detournay and Garagash (2005).

Model geometry and mesh

The model's dimensions are 45 m x 30 m and the mesh is regular with 75 elements in each direction, as seen in Figure 5.1. An initial fracture of 1,2 m is placed at half-height on the left side of the model.

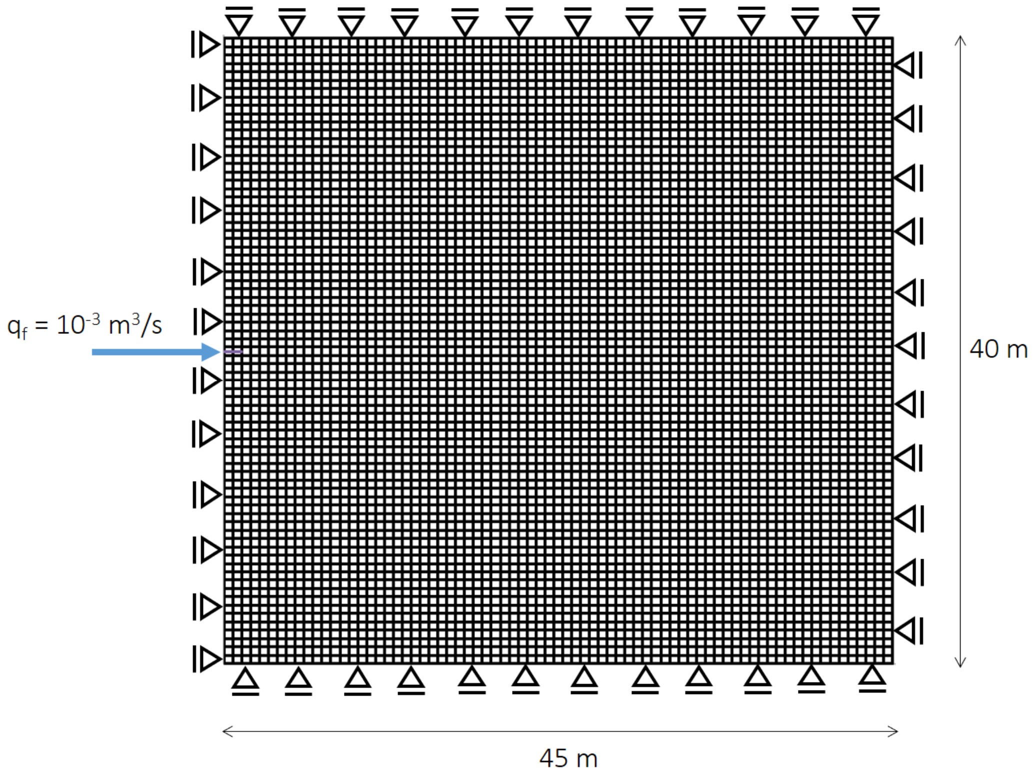

Figure 5.1 – Geometry of the mesh and boundary conditions

Material properties

The material properties are presented in Table 5.1 and Table 5.2. Considering that the KGD K-vertex storage-toughness solution is valid for almost impermeable materials, it is assumed that the rock is impermeable. The parameters are adopted based in the work by Zielonka *et al.* (2014).

Table 5.1 – Hydraulic properties

	Parameter	All Models
Fractures	Initial hydraulic aperture (m)	$2x10^{-3}$
	Fluid Viscosity (kPa.s)	10^{-7}

Table 5.2 – Mechanical properties

	Parameter	
Continuous Region	E (kPa)	$17x10^{7}$
	ν	0,2
	σ_t (kPa) - Numerical	1250
	K_{IC} ($kPa.m^{1/2}$) - Analytical	1460

<u>Boundary and loading conditions</u>

Along the borders of the model the displacements are fixed in the perpendicular direction, as seen in Figure 5.1. The simulations are set to run one single step of 10 s with time increments of size between 0,5 s and 2 s. The fluid injection in the fracture is given by a constant volumetric flux of $1x10^{-3}$ m^3/s at the hydraulic fracture mouth. No in-situ stress state was defined for this analysis.

<u>Results</u>

Figure 5.2 presents the variation of injection pressure, fracture aperture and fracture length over time, for both analytical and numerical solution. It is noticeable that, although some slight differences exist, the results and the tendencies of the numerical model are in good agreement with the analytical solution.

The differences in results may be explained mostly due to three factors. First, it is known how mesh refinement influence the results. As stated by Zielonka et al. (2014), the relative error between solutions decrease monotonically as the mesh is refined. Second, the fact that the model has finite dimensions, in opposition to the infinite medium of the analytical solution, thus leading to possible influence of the boundary conditions at the borders of the model. Third, the theoretical formulations are different. As the KGD solution relies on the stress intensity factor for fracture propagation, the numerical model bases its propagation criterion on the average stress state in a region in the front of the crack tip. As there is no analytical relation between critical stress intensity factor and tensile strength, the solutions may be similar but exact match would only be possible by doing back-analysis to find the correspondent tensile stress.

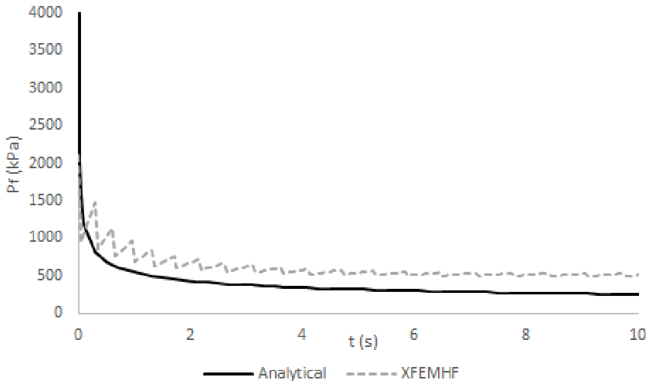

a)

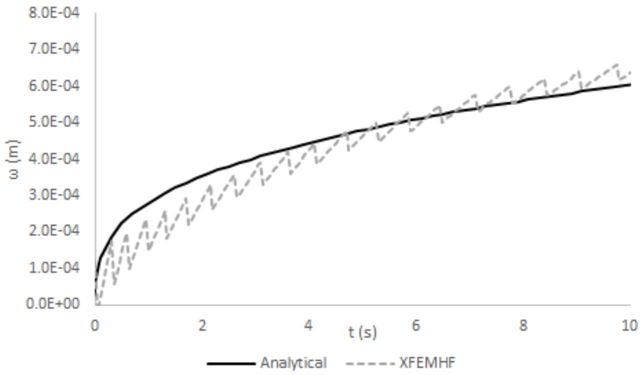

b)

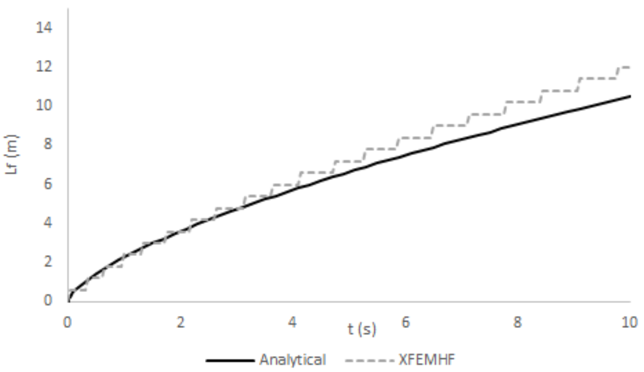

c)

Figure 5.2 – Plots for KGD analytical and numerical solution. a) Injection pressure vs time. b) Fracture maximum aperture vs time. c) Fracture length vs time.

5.2. Flow in a fractured medium

5.2.1. Unidimensional percolation

General description of the simulation

A unidimensional flow simulation of two distinct situations – percolation through (Situation 1) and percolation from (Situation 2) a fracture – may be compared with an analytical solution. Figure 5.3 shows a schematic model for flow through materials with different permeabilities. On the left side of Figure 5.3 a gradient of pore pressure is imposed in the bottom and top of the model ($P_{r,b}$ and $P_{r,t}$), leading to a one-way flow. On the right side of Figure 5.3 a pressure is imposed inside the fracture (P_f) and a gradient is created by imposing a lower pressure on the bottom and top of the model ($P_{r,b}$ and $P_{r,t}$). It is assumed that the filter cake is a layer of infinitesimal length with conductivity equivalent to the fracture face transversal conductivity being $c = k/L$.

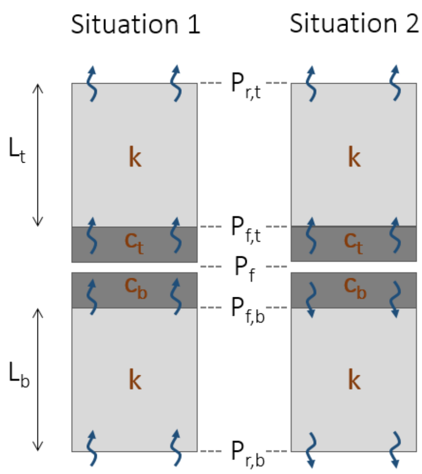

Figure 5.3 – Two situations of unidimensional fluid percolation in a model with different layers. On the left side, percolation from the bottom to the top of the model. On the right side, percolation from the fracture to the porous medium

Considering that the different layers are placed in series, the equivalent resistance (or conductivity) may be computed as

$$k_{eq} = \frac{\sum L}{\sum \frac{L}{k}} \tag{5.1}$$

Therefore, following Darcy's law the volumetric flux in the model is given by

Situation 1	Situation 2
$k_{eq} = \frac{\sum L}{\sum \frac{L}{k}} = \frac{L_b + L_t}{\frac{L_b}{k} + \frac{1}{c_b} + \frac{1}{c_t} + \frac{L_t}{k}}$	$k_{eq} = \frac{\sum L}{\sum \frac{L}{k}} = \frac{L_b}{\frac{L_b}{k} + \frac{1}{c_b}}$
$q = -k\frac{\Delta p}{L} = -k_{eq}\frac{p_{r,t} - p_{r,b}}{L_b + L_t}$	$q = -k\frac{\Delta p}{L} = -k_{eq}\frac{p_{r,t} - p_f}{L_t}$

The pressures may then be computed for both situations as

$$q = -k\frac{p_{r,t} - p_{f,t}}{L_t} \Leftrightarrow p_{f,t} = p_{r,t} - q\frac{L_t}{k}$$

$$q = -k\frac{p_{f,b} - p_{r,b}}{L_b} \Leftrightarrow p_{f,b} = p_{r,b} - q\frac{L_b}{k}$$

$$q = -c_b\left(p_f - p_{f,b}\right) \Leftrightarrow p_f = p_{f,b} - \frac{q}{c_b} \text{ (only for situation 1)}$$

Model geometry and mesh

Given that a unidimensional situation is being modelled, the single element model presented in Figure 5.4 was defined.

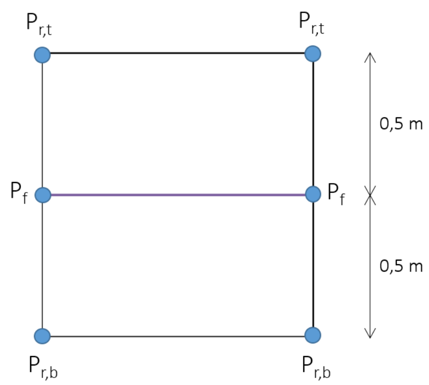

Figure 5.4 – Geometry and boundary conditions of the mesh

Material properties

Six different simulations were defined by changing material properties or boundary conditions. The hydraulic properties both for the porous region and the fractures are presented in Table 5.5.

Table 5.3 – Hydraulic properties

		Situation 1			Situation 2		
	Parameters	**Case 1**	**Case 2**	**Case 3**	**Case 4**	**Case 5**	**Case 6**
Porous Region Hydraulic Conductivity	$k = k_x = k_y$ (m/s)	10^{-8}					
Fracture face transversal conductivity.	c_{top} (m/s.kPa^{-1})	1	10^{-8}	10^{-13}	1	10^{-8}	10^{-10}
	c_{bottom} (m/s.kPa^{-1})						10^{-8}

Boundary and loading conditions

The flow regime is guaranteed by imposing constant pressures in the bottom and the top of the model (and also in the fracture, in Situation 2), following the values presented in Table 5.4. Considering that a permanent regime occurs, the time interval and the number of steps are indifferent.

Table 5.4 – Model boundary conditions

	Situation 1			Situation 2		
	Case 1	**Case 2**	**Case 3**	**Case 4**	**Case 5**	**Case 6**
$P_{r,b}$ (kPa)	1000			0		
$P_{r,t}$ (kPa)	0			0		
P_f (kPa)	-			1000		

Results

The pressure profiles along a vertical section of the model are presented in Figure 5.5. It is evident that the numerical simulation results match exactly the analytical solutions. When the fluid flows from the bottom to the top of the model (situation 1) it is noticeable how the decrease of the fracture face transversal conductivity *c* increases the jump of pressure between the fracture faces. When the injection is made from the fracture (situation 2) the XFEM element is capable of simulating both the loss of pressure in the fracture faces (filter cake) and through the porous medium. Results of Calculation 6 show how different fracture face transversal conductivity in the top and bottom faces of the fracture influence the pressure profile in both halves of the model.

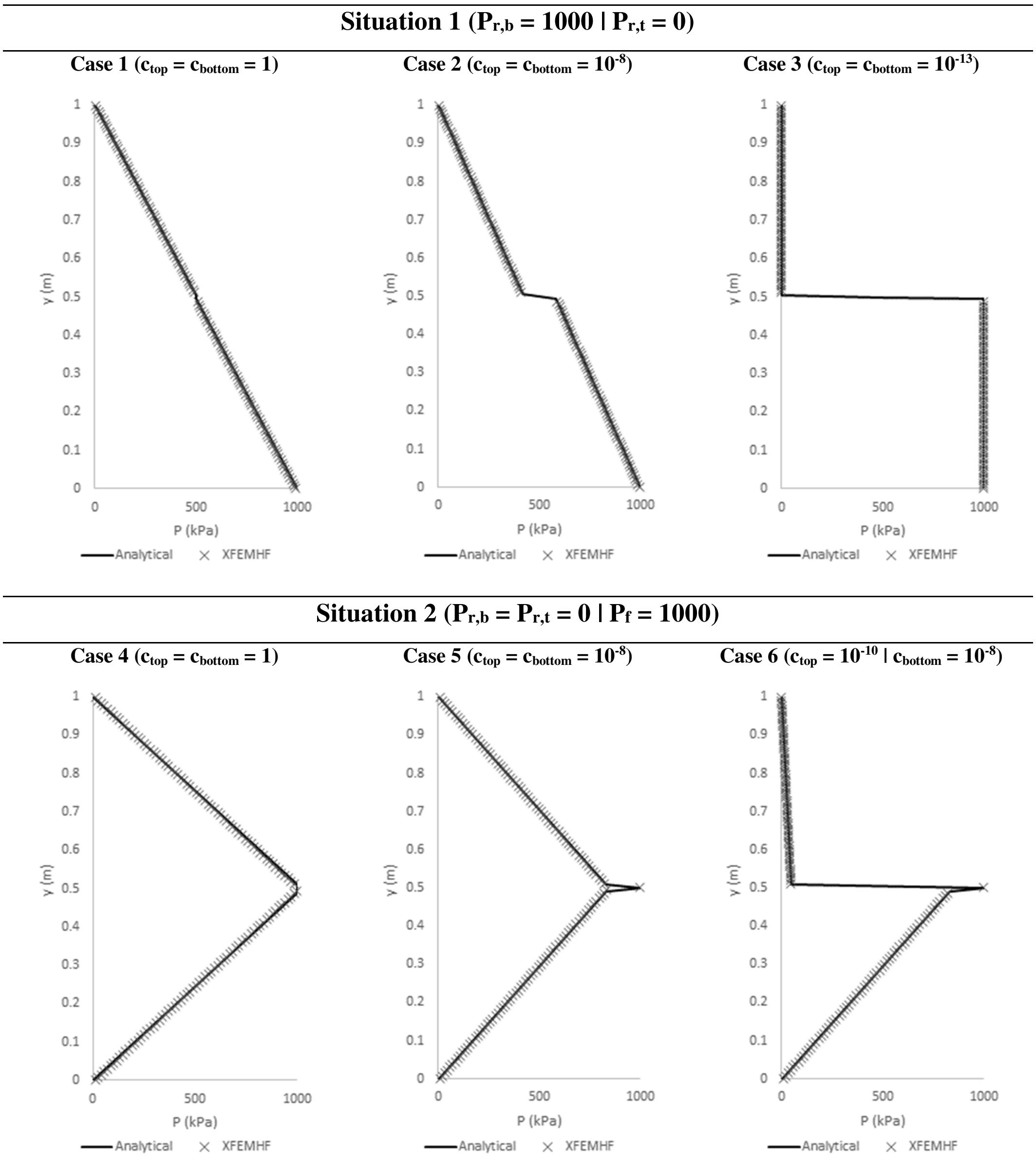

Figure 5.5 – Pressure profiles of the model and analytical solution for each calculation

5.2.2.
Injection in fracture intersection

General description of the simulation

This model contemplates two intersecting fractures with a flow injection in the intersection. The pressure gradient between the injection point and the porous medium is created by imposing a null pressure in the corner nodes of the model. In this model, only hydraulic variables are considered: pore-pressures and fracture pressures. As there are no deformations in the model, a permanent regime is obtained.

Two calculations are performed with variation of the fracture faces transversal conductivity. The results are compared with an Abaqus model with interface elements.

Model geometry and mesh

The model is symmetric, both in horizontal and vertical direction. Its dimensions are 10 m x 10 m and the mesh is regular with 15 elements in each direction, as seen in Figure 5.6.

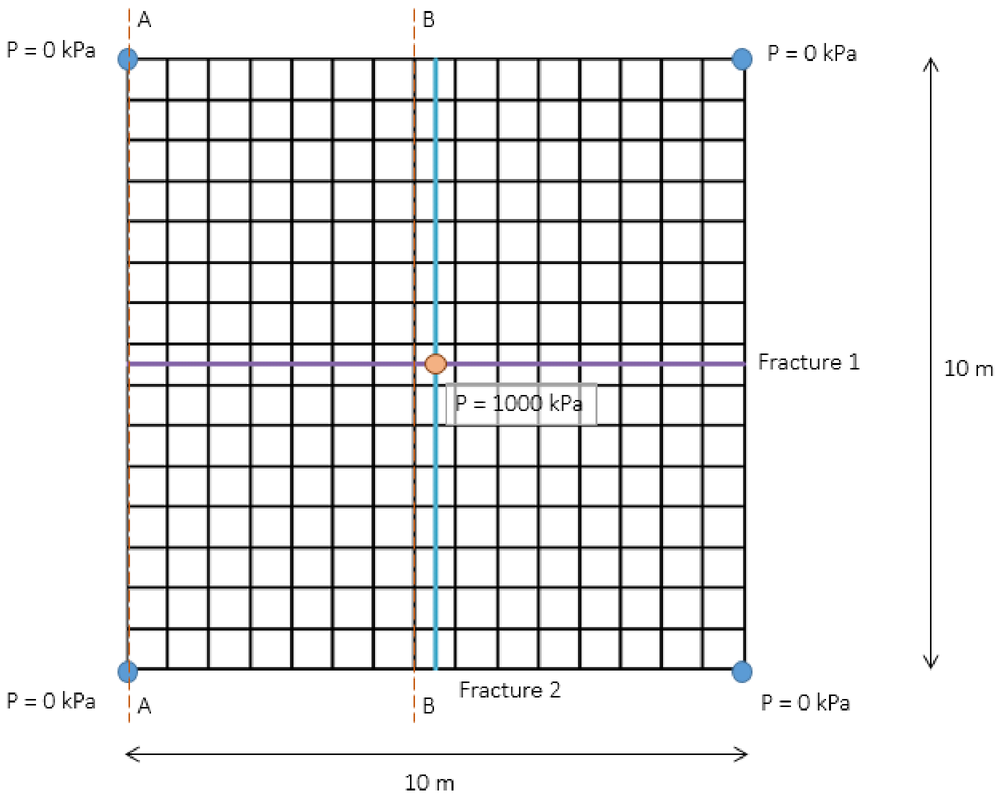

Figure 5.6 – Geometry of the mesh and boundary conditions

Material properties

The hydraulic properties both for the porous region and the fractures are presented in Table 5.5. An isotropic hydraulic conductivity and equal fracture face transversal conductivity for every fracture are used.

Table 5.5 – Hydraulic properties

<table>
<tr><th></th><th>Parameter</th><th>Case 1</th><th>Case 2</th></tr>
<tr><td>Porous Region</td><td>Hydraulic conductivity:
$k = k_x = k_y$ (m/s)</td><td colspan="2">10^{-8}</td></tr>
<tr><td rowspan="3">Fracture</td><td>Fracture face transversal conductivity:
$c = c_{top} = c_{bottom}$ (m/s.kPa^{-1})</td><td>10^{-12}</td><td>10^{-9}</td></tr>
<tr><td>Hydraulic aperture (m)</td><td>$2x10^{-3}$</td><td>$2x10^{-3}$</td></tr>
<tr><td>Fluid Viscosity (kPa.s)</td><td colspan="2">10^{-6}</td></tr>
</table>

Boundary and loading conditions

The flow regime is guaranteed by imposing a constant pressure in the fracture intersection of 1000 kPa and a pressure of 0 kPa in the corners of the node, as indicated in Figure 5.6. Considering that a permanent regime occurs, the time interval and the number of steps are indifferent.

Results

Figure 5.7 shows the pore-pressure fields for the two calculations run, as well as the results obtained using Abaqus with interface elements. Figure 5.8 presents the values of the pore-pressures along the sections A-A and B-B (defined in Figure 5.6). It is easily noticeable that the comparison of the two simulation tools shows a very good agreement. Slightly differences are due to the way the different output tools plot their results.

As the porous medium and the fracture longitudinal transmissibility are the same in both calculations, the change in the fracture face transversal conductivity strongly affects the pore-pressure fields. For lower values of the coefficient (Case 1: $c = 10^{-12}$) a drop of pressure from 1000 kPa to around 30 kPa occurs between the fracture and the porous medium in both sections. On the other hand, a much smaller drop of pressure is verified in Case 2, since the increase of the coefficient obviously reduces the gradient.

Overall, it is shown that the implemented code is able to simulate the effect of the hydraulic behaviour in intersection of fractures and the leak-off to the porous region.

Case 1 ($c = 10^{-12}$)

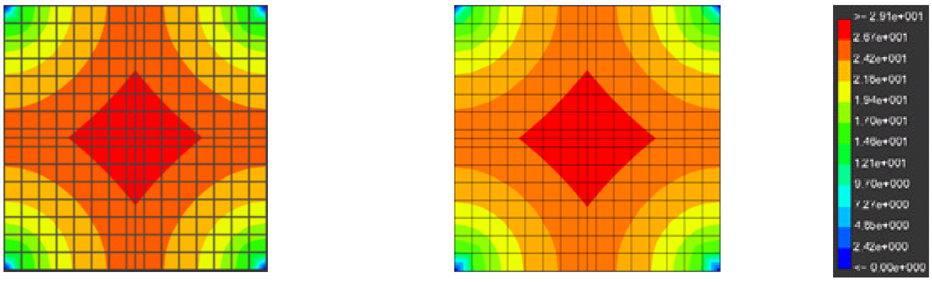

XFEMHF Abaqus

Case 2 ($c = 10^{-9}$)

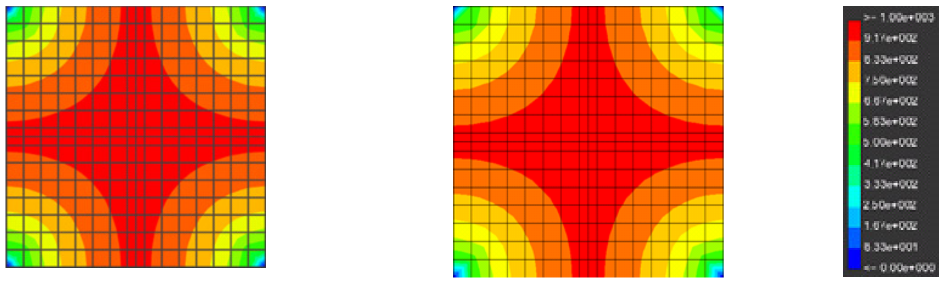

XFEMHF Abaqus

Figure 5.7 – Pore-pressure fields

Case 1 ($c = 10^{-12}$)

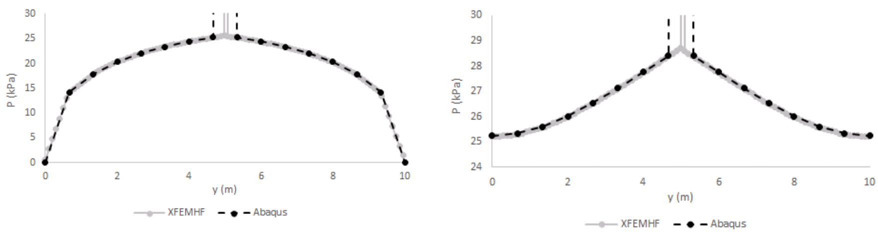

Section A-A Section B-B

Case 2 ($c = 10^{-9}$)

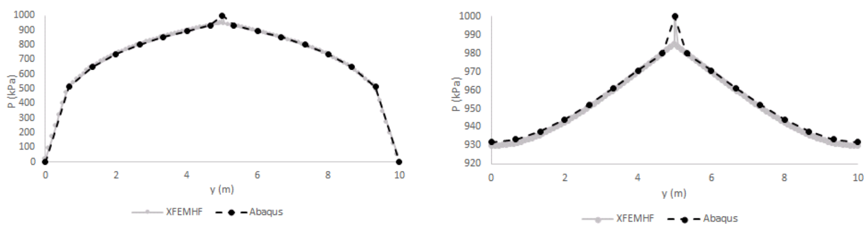

Section A-A Section B-B

Figure 5.8 – Pore-pressures in sections A-A and B-B

5.2.3.
Percolation through a fractured medium

General description of the simulation

In this model, four randomly orientated fractures intersect each other. A pressure gradient is created. Only the hydraulic variables are considered: pore-pressures and fracture pressures, obtaining a permanent regime. Four calculations are performed with variation of the fracture face transversal conductivity and the fracture hydraulic aperture. The results are compared with a model where the fractures are represented by interface elements.

Model geometry and mesh

The model dimensions are 30 m x 15 m and the mesh is regular with 30 and 15 elements in the horizontal and vertical directions, respectively, as seen in Figure 5.9. The fractures have different orientations and lengths that were defined randomly.

Figure 5.10 shows the mesh with interface elements represented in red. A total of 1382 elements are used, where 73 are 4-node two-dimensional cohesive elements (COH2D4P) and 1309 are 4-node bilinear displacement and pore pressure elements (CPE4P).

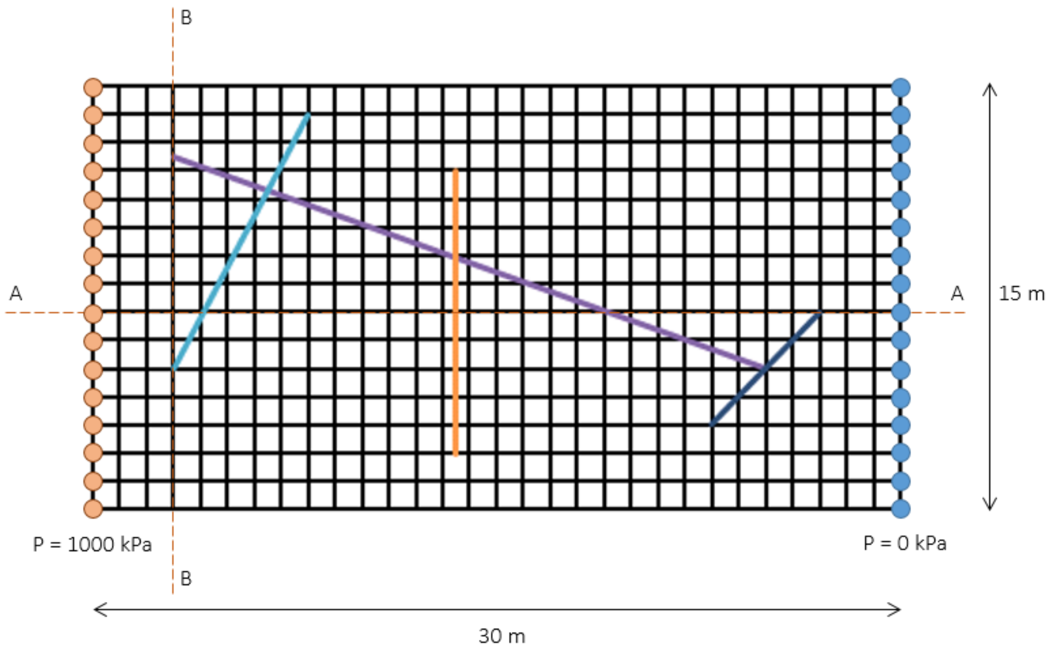

Figure 5.9 – Geometry of the mesh and boundary conditions

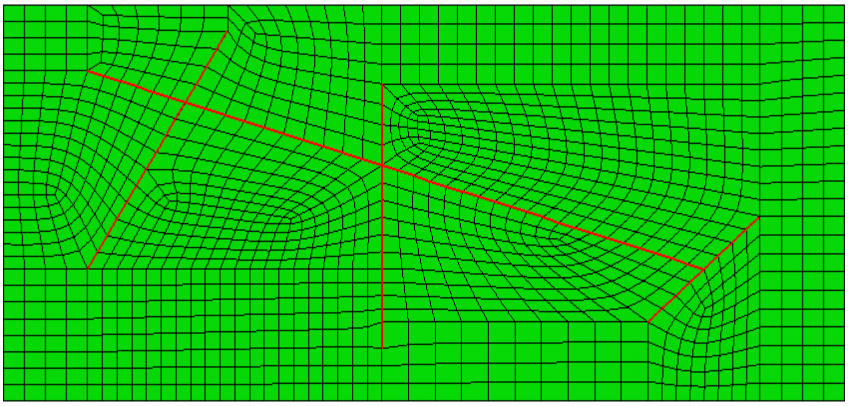

Figure 5.10 – Geometry of the mesh of Abaqus with interface elements model

<u>Material properties</u>

The hydraulic properties both for the porous region and the fractures are presented in Table 5.6. The porous media is isotropic and the fracture face transversal conductivity and hydraulic apertures are the same for every fracture in each of the calculations.

Table 5.6 – Hydraulic properties

	Parameter	**Case 1**	**Case 2**	**Case 3**	**Case 4**
Porous Region	Hydraulic conductivity: $k = k_x = k_y$ (m/s)	10^{-8}			
Fracture	Fracture face transversal conductivity: $c = c_{top} = c_{bottom}$ (m/s.kPa^{-1})	10^{-7}	10^{-7}	10^{-12}	10^{-12}
	Hydraulic aperture (m)	$2x10^{-3}$	$2x10^{-6}$	$2x10^{-3}$	$2x10^{-6}$
	Fluid Viscosity (kPa.s)	10^{-6}			

<u>Boundary and loading conditions</u>

The flow regime is guaranteed by imposing a constant pressure of 1000 kPa at the left border and a null pressure at the right border, as indicated in Figure 5.9. Considering that a permanent regime occurs, the time interval and the number of steps are indifferent.

Results

Figure 5.11 shows the pore-pressure fields for the four simulations, as well as the results obtained using Abaqus with interface elements. Figure 5.12 presents the values of the pore-pressures along sections A-A and B-B defined in Figure 5.9. It is easily noticeable from both figures that the XFEMHF simulations show very good agreement with the interface element solution.

A sensitivity analysis of two parameters – fracture longitudinal transmissibility and fracture face transversal conductivity – shows the strong influence that these have on the pressure fields.

The calculation with higher values of fracture transversal and longitudinal transmissibility (Case 1: $c = 10^{-7} \parallel w_{init} = 2x10^{-3}$) shows that when both permeabilities are high, fluid easily flows to the fractures, showing an effect of "drainage canals". The fluid from the porous region tends to flow to the fracture, reducing the fluxes in the middle part of the model. Then, it leaves the right sided fracture to reach the model border, as seen in Figure 5.13. This effect also proves that the fracture intersections are capable of transmitting the fluid flow between different fractures.

In Case 2 ($c = 10^{-7} \parallel w_{init} = 2x10^{-6}$), the longitudinal transmissibility is reduced by means of the fracture aperture. Keeping a higher transversal conductivity, the flow easily enters or leaves the fractures. However, the drainage effect related with the longitudinal flow no longer occurs. This way, the flow crosses the fractures but does not enter in this preferential path, keeping the same direction in the porous region.

Case 3 ($c = 10^{-12} \parallel w_{init} = 2x10^{-3}$) and Case 4 ($c = 10^{-12} \parallel w_{init} = 2x10^{-3}$) show that the reduction of the fracture face transversal conductivity decreases the transversal conductivity to a point that the flow is no longer capable of entering the fractures. Therefore, the fractures represent a barrier and the fluid has to deviate to continue to flow through the porous region, as seen in Figure 5.13. Despite the difference in the longitudinal transmissibility between Case 3 and Case 4, there is no significant difference in the results, as the flow does not flow along the fractures.

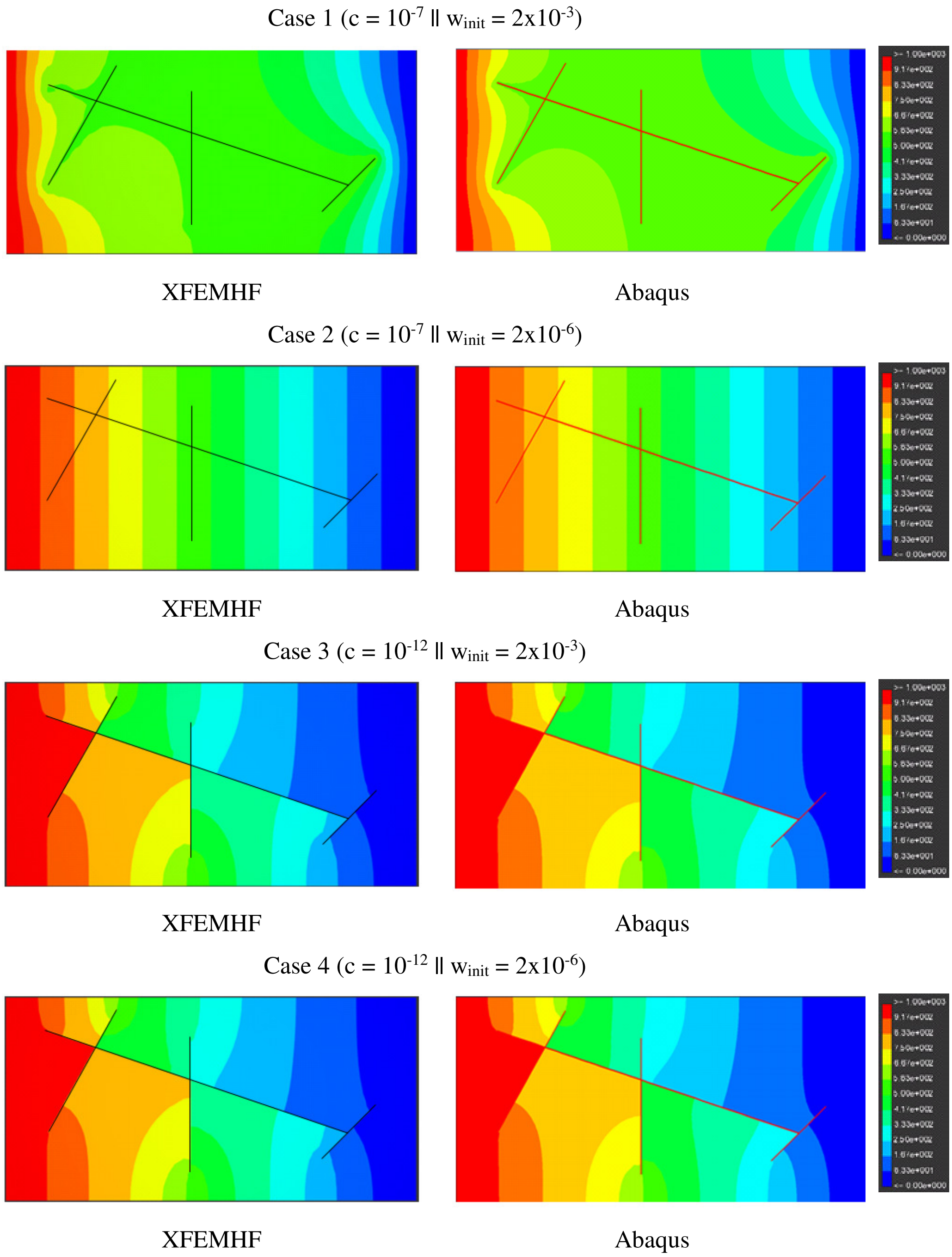

Figure 5.11 – Pore-pressure fields

Case 1 ($c = 10^{-7}$ || $w_{init} = 2x10^{-3}$)

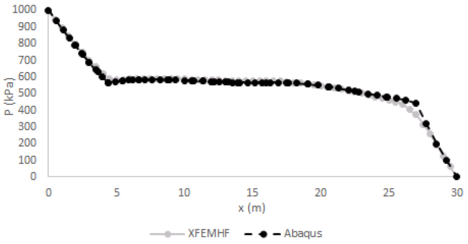

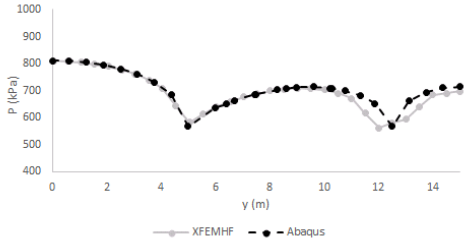

Section A-A

Section B-B

Case 2 ($c = 10^{-7}$ || $w_{init} = 2x10^{-6}$)

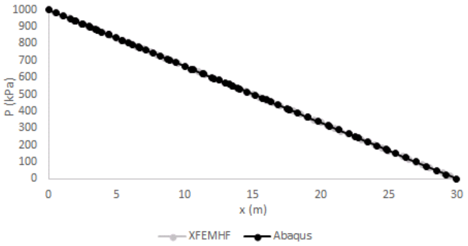

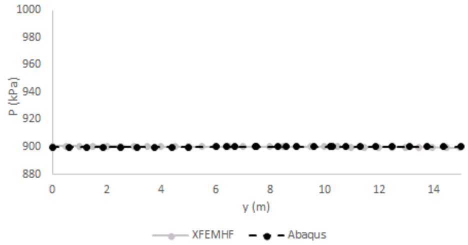

Section A-A

Section B-B

Case 3 ($c = 10^{-12}$ || $w_{init} = 2x10^{-3}$)

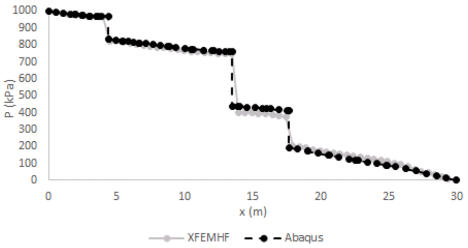

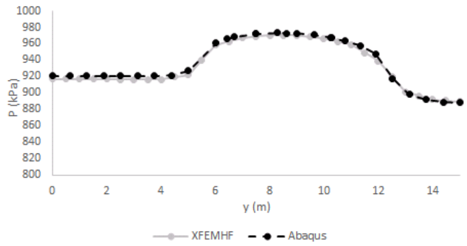

Section A-A

Section B-B

Case 4 ($c = 10^{-12}$ || $w_{init} = 2x10^{-6}$)

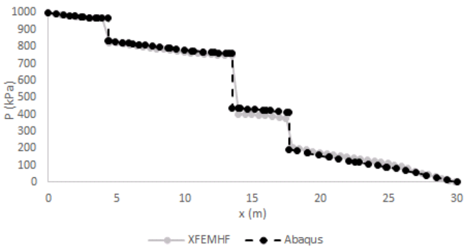

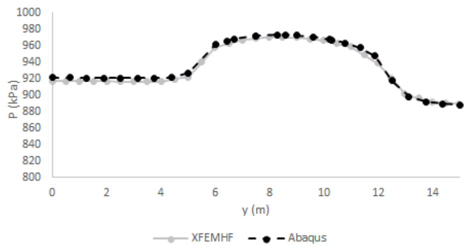

Section A-A

Section B-B

Figure 5.12 – Pore-pressures in sections A-A and B-B

Case 1 ($c = 10^{-7}$ || $w_{init} = 2x10^{-3}$)

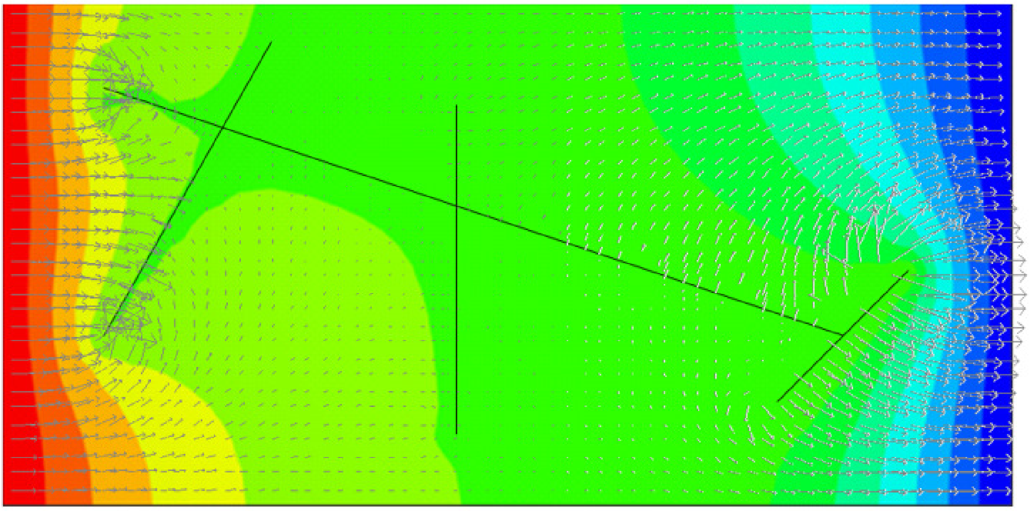

Case 4 ($c = 10^{-12}$ || $w_{init} = 2x10^{-6}$)

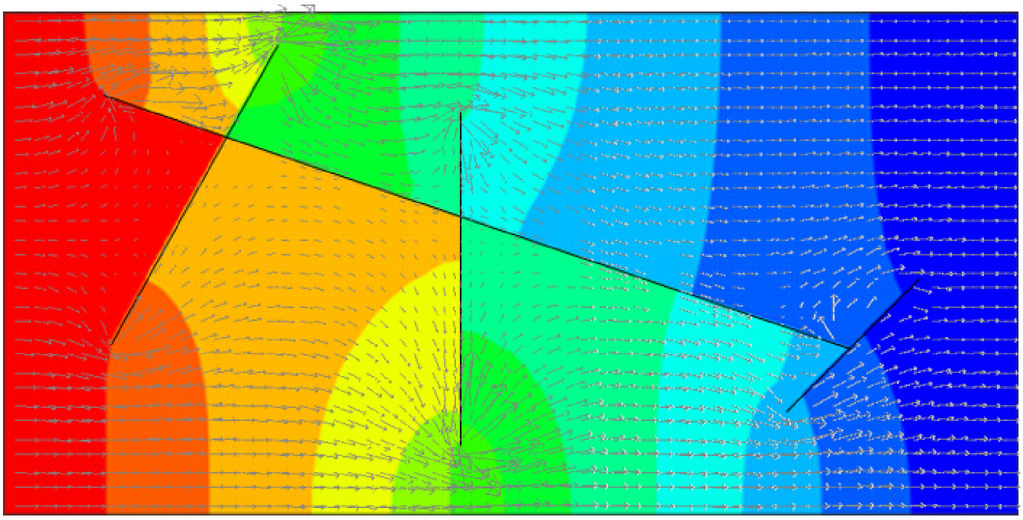

Figure 5.13 – Flow vectors along the model

5.2.4. Consolidation in a fractured medium

<u>**General description of the simulation**</u>

In this model, a distributed uniform load is applied at the top of the model while the pressure is imposed to be zero in the same border. All the physics are considered and coupled: displacements, pore-pressures and fracture pressures, obtaining a transient regime. The displacement boundary conditions are set to the model to represent a unidimensional consolidation problem. However, four randomly orientated and intersected fractures exist in the model. Four calculations are performed with variation of the fracture face transversal conductivity and the fracture hydraulic aperture. The results are compared with a model with interface elements generated and run in the software GeMA (Mendes, Gattass and Roehl, 2016).

Model geometry and mesh

This model has the same geometry as the one presented in Chapter 5.2.3. The model's dimensions are 30 m x 15 m and the mesh is regular with 30 and 15 elements in the horizontal and vertical directions, respectively, as seen in Figure 5.14. The fractures have different orientations and lengths that were defined randomly.

Figure 5.15 shows the mesh used in the GeMA simulation, with the interface elements represented in red. The mesh was generated by the software Sigma2D (Miranda and Martha, 2017) and total of 1382 elements are used, where 73 are 4-node two-dimensional cohesive elements and 1309 are 4-node bilinear displacement and pore pressure elements.

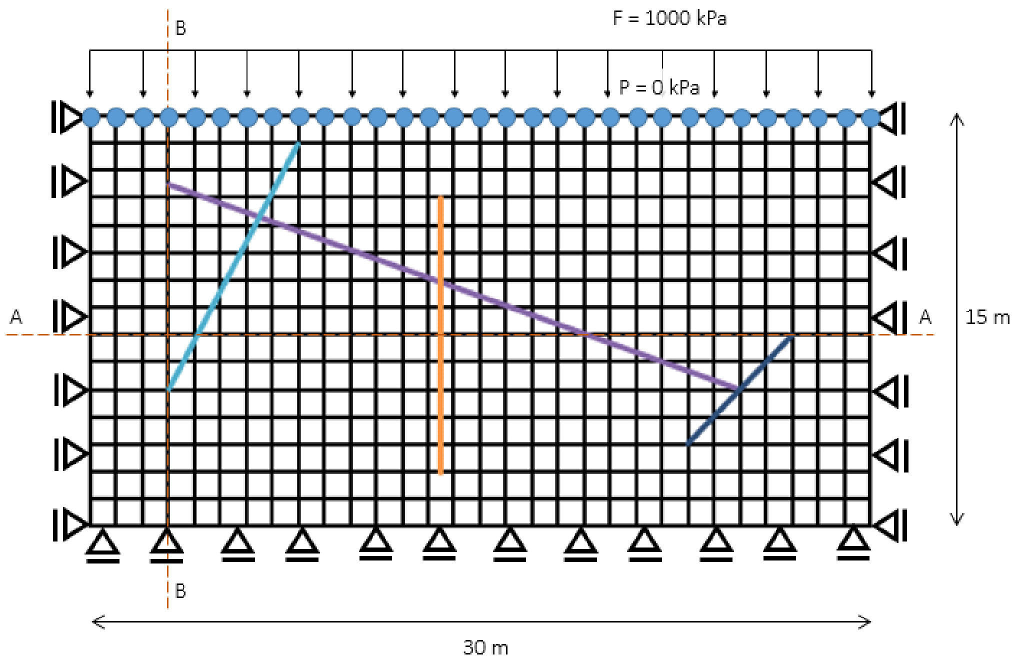

Figure 5.14 – Geometry of the mesh and boundary conditions

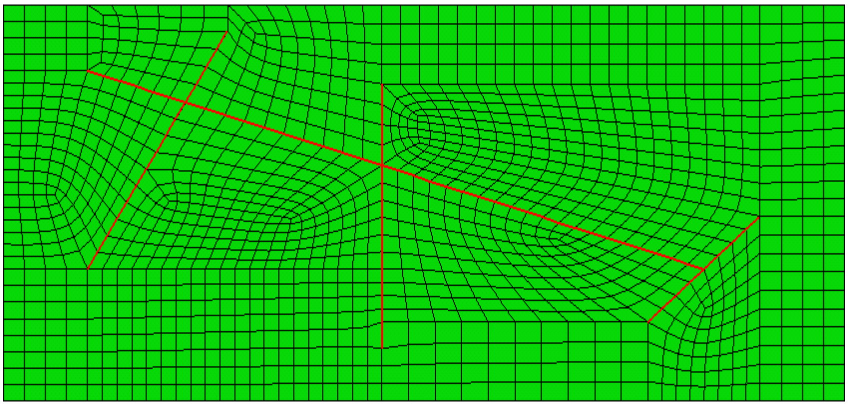

Figure 5.15 – Geometry of the mesh of GeMA with interface elements model

<u>**Material properties**</u>

The hydraulic properties both for the porous region and the fractures are presented in Table 5.6. An isotropic hydraulic conductivity is used in the porous medium. The fracture face transversal conductivity and initial hydraulic apertures are the same for every fracture in each of the calculations and the variation between analyses is similar to the one presented in Chapter 5.2.3. As this model contemplates deformations, the hydraulic aperture changes during the simulation.

Table 5.7 – Hydraulic properties

	Parameter	**Case 1**	**Case 2**	**Case 3**	**Case 4**
Porous Region	Hydraulic conductivity: $k = k_x = k_y$ (m/s)	10^{-8}			
Fracture	Fracture face transversal conductivity: $c = c_{top} = c_{bottom}$ (m/s.kPa^{-1})	10^{-7}	10^{-7}	10^{-14}	10^{-14}
	Initial hydraulic aperture (m)	$2x10^{-3}$	$2x10^{-6}$	$2x10^{-3}$	$2x10^{-6}$
	Fluid Viscosity (kPa.s)	10^{-6}			

The mechanical properties of the porous region are defined in Table 5.8. The fractures have a traction free behaviour. However, if subjected to compression, the contact between faces is modelled.

Table 5.8 – Mechanical properties

	Parameter	**Case 1**	**Case 2**	**Case 3**	**Case 4**
Porous Region	E (kPa)	$40x10^3$			
	ν	0,3			

Boundary and loading conditions

To simulate an effect similar to a unidimensional consolidation problem the bottom border of the model is fixed in the vertical direction, while the right and left borders are restrained to horizontal displacements. The displacement of the model is guaranteed by a uniform distributed load of 1000 kPa in the top border. As for hydraulic boundary conditions, the top border is fixed to a pressure of 0 kPa.

The previous mentioned boundary conditions are applied in a first step with a time interval of 10^{-7} s. This very small time interval may be considered as an instantaneous application of the load, guaranteeing that consolidation practically does not occur during the step.

The loads and boundary conditions are then kept constant for 50 varying time intervals, while consolidation occurs.

Results

Figure 5.16 shows the pore-pressure fields for the four simulations at the same time ($t = 95 \text{ x } 10^5$ s), as well as the results obtained using GeMA with interface elements. Figure 5.17 presents the values of the pore-pressures along the sections A-A and B-B (defined in Figure 5.14). It is easily noticeable from both figures that the XFEMHF simulations show a very good agreement with the GeMA built-in with interface elements.

Similarly to Chapter 5.2.3, a very simple sensitivity analysis of two parameters – fracture longitudinal transmissibility and fracture face transversal conductivity – shows the strong influence that these have in the pressure fields and model behaviour.

The calculation with higher values of fracture transversal and longitudinal transmissibility (Case 1: $c = 10^{-7} \parallel w_{init} = 2x10^{-3}$) shows that when both permeabilities are high, then fluid easily flows to the fractures, which have an effect of "drainage canals". The fluid from the porous region tends to flow to the fracture, reducing the pore pressures drastically in the vicinity of the fractures. Figure 5.18

shows how the fractures work as drains, collecting fluid from the more pressurized regions to as near as closer to the top border. This effect also proves that the fracture intersections are capable of transmitting the fluid flow between different fractures. This way, it should be expected that with influence of the "drains", the consolidation occurs faster that in a standard unidimensional consolidation, as seen in Figure 5.19

In Case 2 ($c = 10^{-7}$ || $w_{init} = 2x10^{-6}$), the longitudinal transmissibility is reduced by means of the fracture aperture. Keeping a higher transversal conductivity, the flow easily enters or leaves the fractures. However, the drainage effect related with the longitudinal flow no longer occurs, due to the reduction of longitudinal transmissibility. This way, the flow crosses the fractures but does not enter in this preferential path, keeping the same direction in the porous region. The lack of influence of the fractures is visible in Figure 5.19, as the curve for this calculation overlaps the standard unidimensional consolidation solution.

In Case 3 ($c = 10^{-14}$ || $w_{init} = 2x10^{-3}$) and Case 4 ($c = 10^{-14}$ || $w_{init} = 2x10^{-3}$) it is shown that the reduction of the fracture face transversal conductivity decreases the transversal conductivity to a point that the flow is no longer capable of entering the fractures. Therefore, the fractures represent a barrier and the fluid has to deviate to continue to flow along the porous region. As seen in Figure 5.18, the flow is almost inexistent under the group of fractures. Despite the difference in the longitudinal transmissibility between Case 3 and Case 4, there is no significant difference in the results, as the flow does not flow along the fractures. The influence that the reduction of fracture transversal flow has in the model is visible in Figure 5.19, as the time vs deformation curve shows that in Case 3 and 4 the sample takes more time to consolidate.

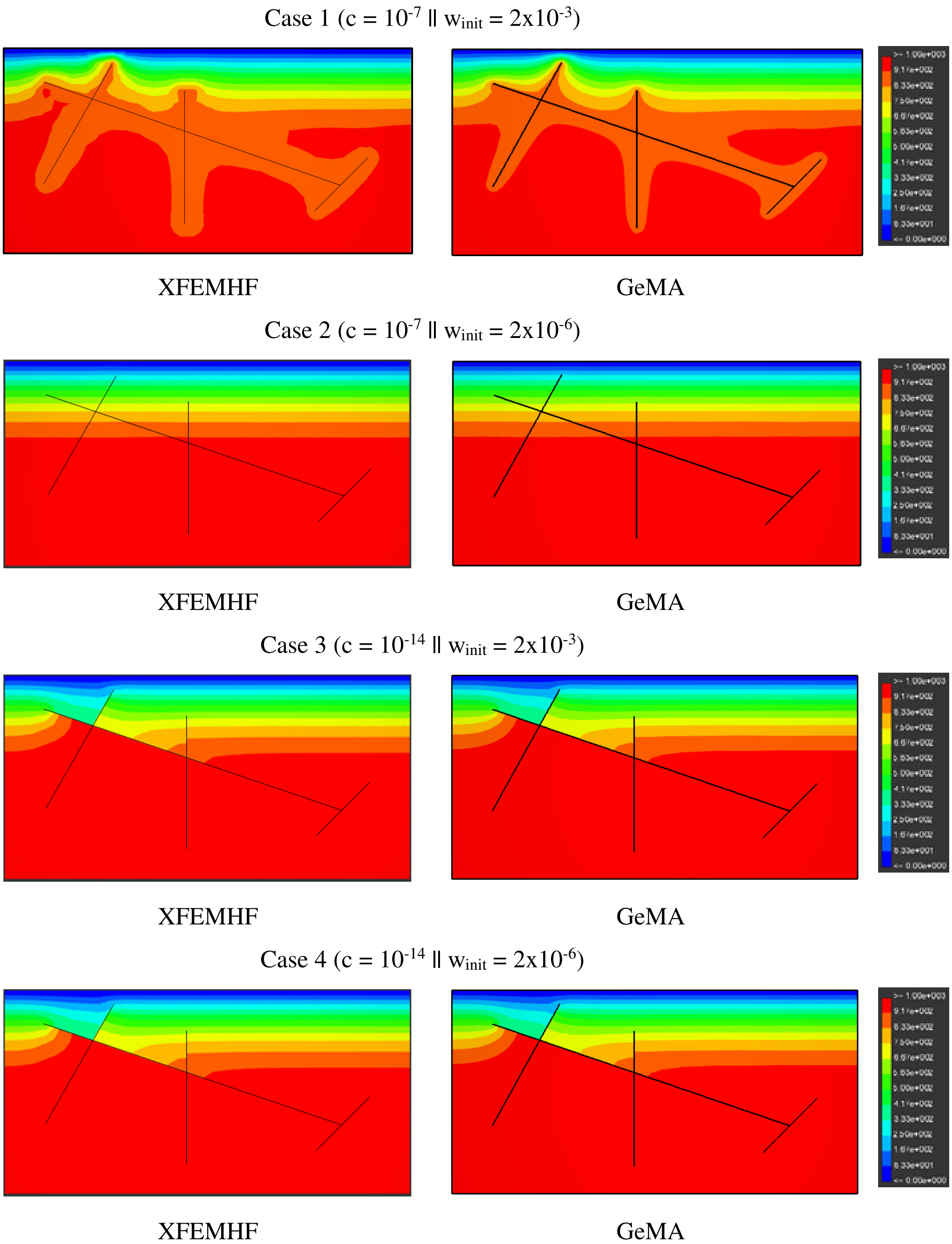

Figure 5.16 – Pore-pressure fields at time 95 x 10^5 s

Case 1 ($c = 10^{-7}$ || $w_{init} = 2x10^{-3}$)

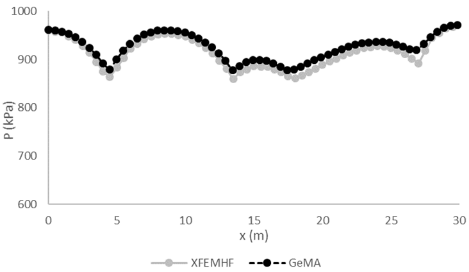

Section A-A

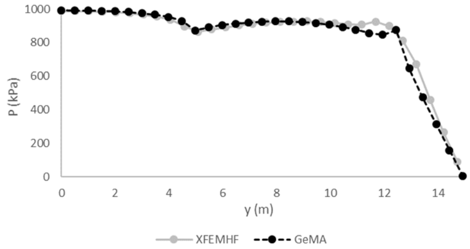

Section B-B

Case 2 ($c = 10^{-7}$ || $w_{init} = 2x10^{-6}$)

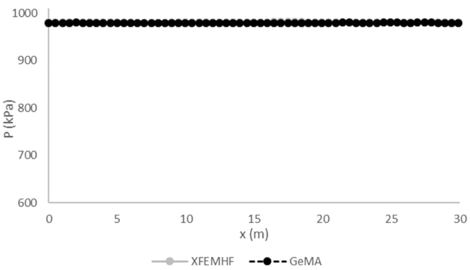

Section A-A

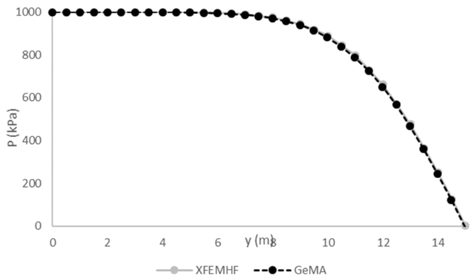

Section B-B

Case 3 ($c = 10^{-14}$ || $w_{init} = 2x10^{-3}$)

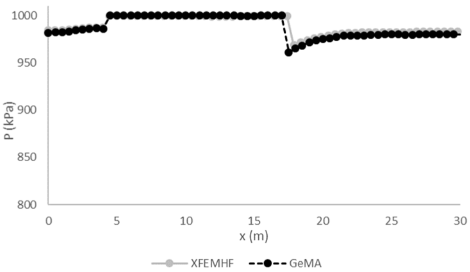

Section A-A

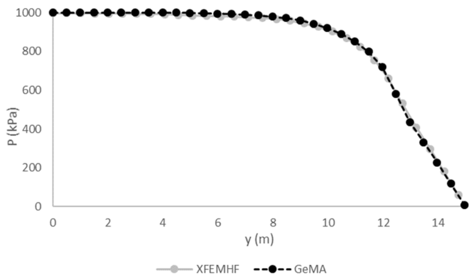

Section B-B

Case 4 ($c = 10^{-14}$ || $w_{init} = 2x10^{-6}$)

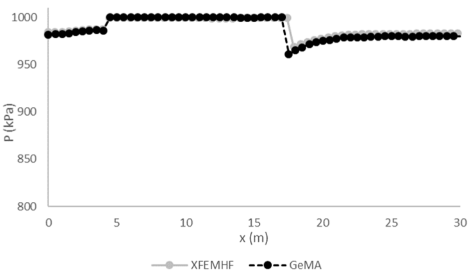

Section A-A

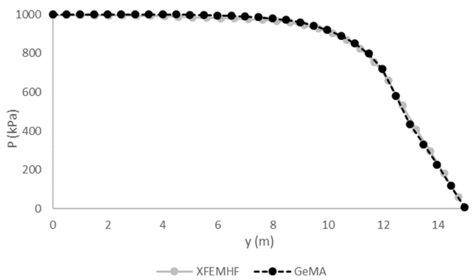

Section B-B

Figure 5.17 – Pore-pressures in sections A-A and B-B at time 95 x 10^5 s

Case 1 (c = 10^{-7} || $w_{init} = 2x10^{-3}$)

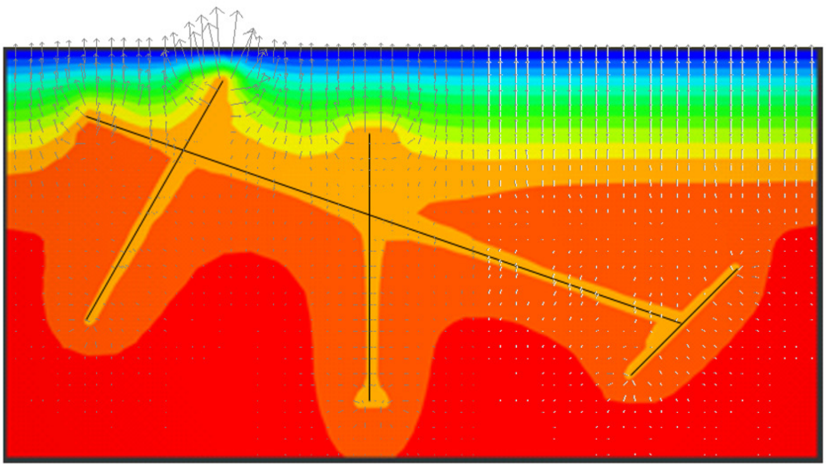

Case 4 (c = 10^{-14} || $w_{init} = 2x10^{-6}$)

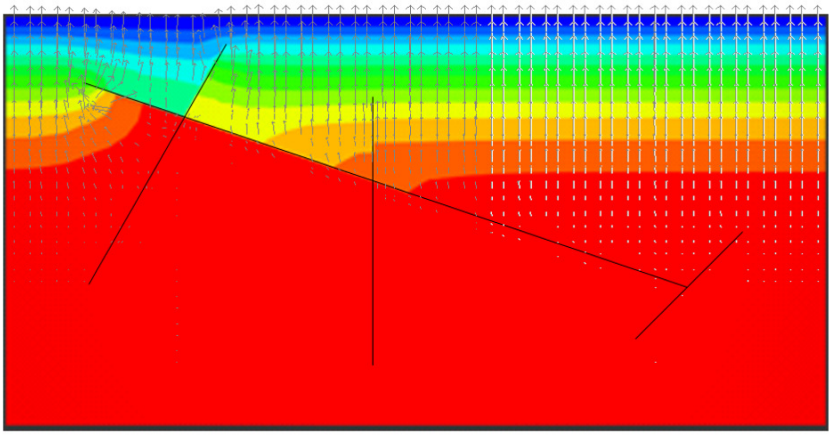

Figure 5.18 – Flow vectors along the model at time 95 x 10^5 s

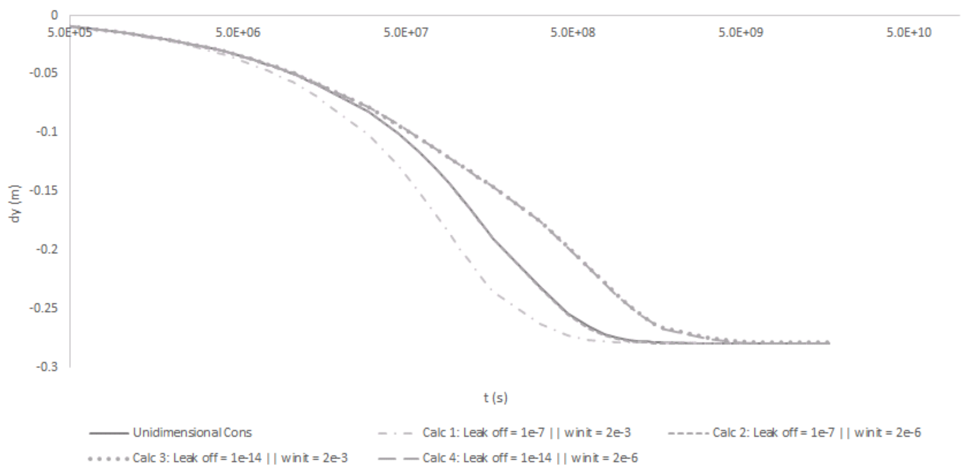

Figure 5.19 – Vertical displacement in the top border's mid-point for all four analyses with XFEMHF

5.3.
Contact and friction

5.3.1.
Single element with horizontal fracture

5.3.1.1. Vertical cyclic load

<u>**General description of the simulation**</u>

The objective of this simulation is to show in a simplistic manner how the implemented contact model works. A cyclic prescribed displacement is applied in the top of a single element with one horizontal fracture and the fracture behaviour depends on its relative position. If the fracture faces touch each other, contact exists. If not, fracture faces move independently. In this simulation only mechanical degrees of freedom are used.

<u>**Model geometry and mesh**</u>

The model has a single square element with dimensions 1,0 m x 1,0 m, as seen in Figure 5.20. The fracture is horizontal at half-height of the element.

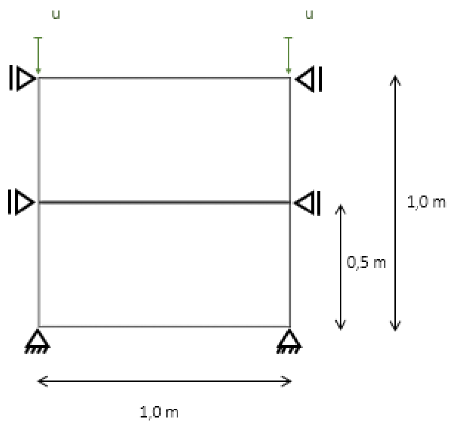

Figure 5.20 – Geometry of the mesh and boundary conditions

<u>**Material properties**</u>

The mechanical properties of the solid region are defined in Table 5.9. The fractures have a traction free behaviour. However, if subjected to compression, the contact between faces is modelled using a penalty parameter of 10^{11} kPa.

Table 5.9 – Mechanical properties

	Parameter	Value
Solid Region	E (kPa)	10^6
	ν	0,3

Initial conditions

To assess the effect of initial stresses in the contact behaviour, two distinct calculations are made, one without initial stresses and other with an initial vertical stress of 500 kPa.

Boundary and loading conditions

The boundary conditions are set in order that only vertical displacements occur in the model, as seen in Figure 5.20. A prescribed vertical displacement at the top of the model, *u*, is applied in 65 increments of a fixed length of 1 second each and follows the sinusoidal function presented in Figure 5.21. It must be reminded that, although the notion of time is used, the calculation in each increment is static.

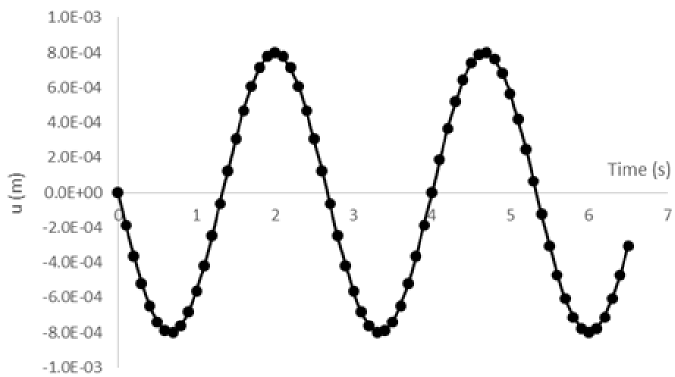

Figure 5.21 – Prescribed vertical displacement at the top of the model

Results

The results show that the contact model simulates the effect of contact between faces correctly. Figure 5.22 shows a set of frames taken from the deformed mesh at the end of 8 increments, with the undeformed mesh being represented by grey dashed lines. In both models it is visible that when contact exists in the fracture faces, the compression in the continuous region is transmitted and the whole model deforms monolithically (see t = 0,3 s and t = 2,9 s). It is also noticeable that when the fracture faces are not in contact, the upper half of the model translates vertically without affecting the lower half (see t = 1,6 s, t = 2,0 s and t = 2,6 s). The main difference between the simulations with and without in-situ stress is visible in increment t = 1,4 s. In the case without in-situ stress, a positive displacement at the top of the model results in an opening of the fracture. On the other hand, when in-situ stresses exist, the before fracture opening the model expands to relieve the initial stresses. This way, as seen in t = 1,4 s the two element halves are still in contact and therefore the fracture opening will be smaller.

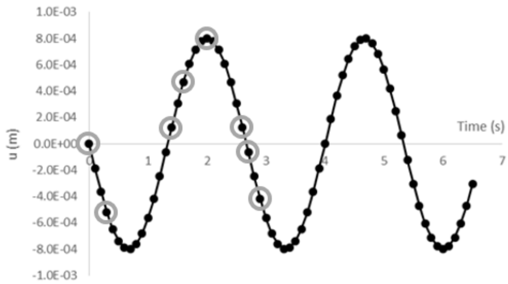

a)

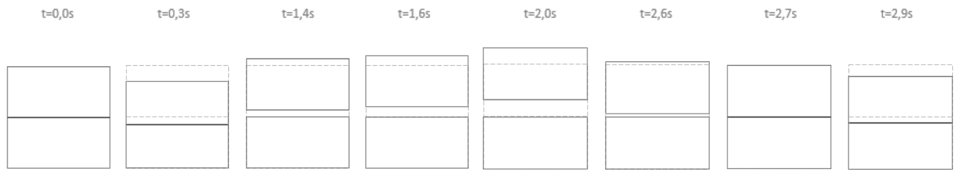

b)

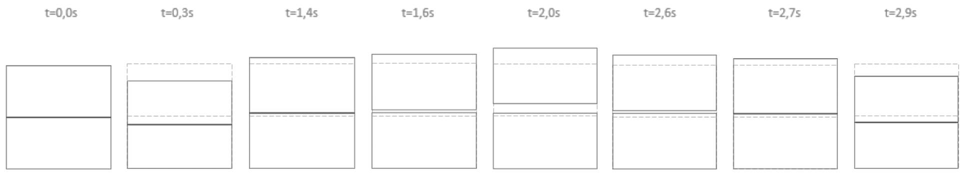

c)

Figure 5.22 – Deformed mesh at the end of 8 increments. a) Time increments represented. b) Model without in-situ stress. c) Model with in-situ stress of 500 kPa

Figure 5.23 gives further insight about the contact behaviour. As expected, while in compression, the fracture opening assumes a very small negative value, which can be considered zero, i.e. the fracture faces are in contact. When the fracture faces move apart, there is no stress transmission between the two halves of the model. Consequently, the vertical stress in the continuous region is reduced to zero.

As stated previously, the expansion due to the stress relief in the model with initial stresses results in a smaller fracture opening (see Figure 5.23a). Therefore, the contact and the compressive stresses in the model occur in longer periods, as seen in Figure 5.23b.

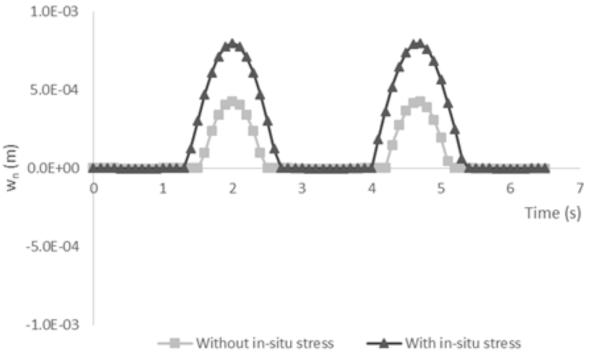

a)

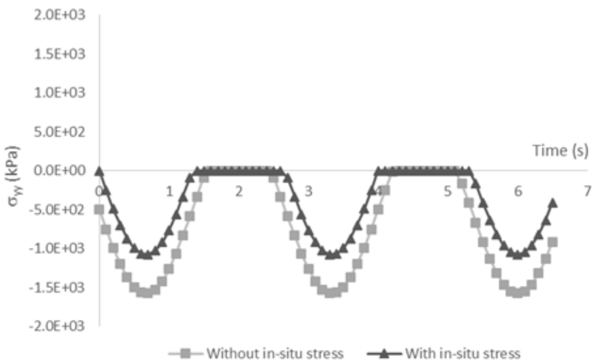

b)

Figure 5.23 – Fracture opening (a) and vertical stress in the continuous region (b)

Finally, it is visible in Figure 5.24 that the initial normal stress in the fracture is correctly computed, as a value of 500 kPa is obtained in the first increment of Figure 5.24b. It may also be stated that the penalty method correctly represents the effect of compression when in contact and a stress-free situation when the fracture opens.

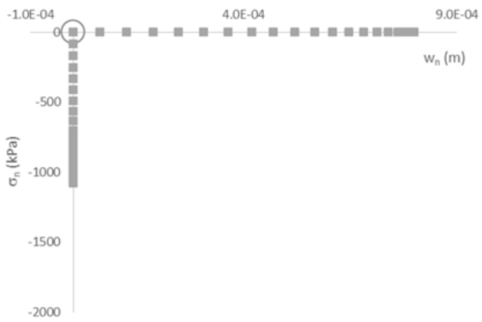

a) **b)**

Figure 5.24 – Fracture opening vs Normal stress in the fracture for every increment (grey circle points the first increment). a) Simulation without in-situ stress. b) Simulation with in-situ stress

5.3.1.2. Horizontal load

<u>**General description of the simulation**</u>

This model shows how the implemented contact and friction models work. A horizontal prescribed displacement is applied in the upper half of a single element with one horizontal fracture. The boundary conditions are defined in a way that only shear stress occur, and different initial stress conditions are defined to confirm the effect that confinement has in shear strength.

<u>**Model geometry and mesh**</u>

The model has a single square element with dimensions 1,0 m x 1,0 m, as seen in Figure 5.25. The fracture is horizontal at half-height of the element.

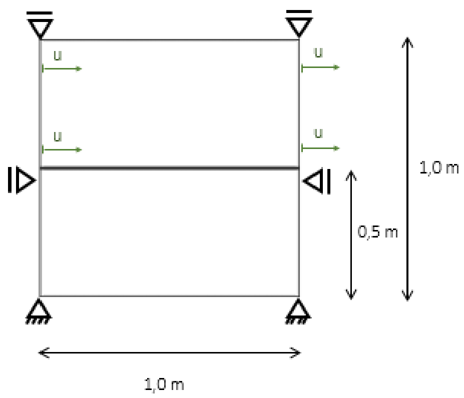

Figure 5.25 – Geometry of the mesh and boundary conditions

Material properties

The mechanical properties of the solid region and the fracture are defined in Table 5.10. The fracture has a friction behaviour given by the Mohr Coulomb model. A non-associated law is used, i.e. no dilatation occurs due to shear deformations.

Table 5.10 – Mechanical properties

	Parameter	Value
Solid Region	E (kPa)	10^6
	ν	0,3
Fracture	K_n (kPa)	0^{**}
	K_s (kPa)	10^7
	ϕ' (°)	35
	c' (kPa)	0

**value in traction. In compression, a penalty factor is applied

Initial conditions

To assess the effect of the confinement stresses in the friction behaviour, six distinct initial stresses are defined, as seen in Table 5.11.

Boundary and loading conditions

The defined boundary conditions (see Figure 5.25) fix the lower half of the model in every direction, while the upper half is only able to translate horizontally. After a first step for definition of initial stress, a horizontal displacement is prescribed and subdivided in 20 increments. In the first three tests a positive displacement is applied, while in the other three tests a negative value is used, as seen in Table 5.11.

Table 5.11 – Prescribed horizontal displacement and initial vertical stress

	Initial vertical stress (kPa)	Prescribed horizontal displacement (m)
Test 1	-1346,1	$5x10^{-4}$
Test 2	-2692,3	$5x10^{-4}$
Test 3	-4038,4	$5x10^{-4}$
Test 4	-673,1	$-5x10^{-4}$
Test 5	-2019,2	$-5x10^{-4}$
Test 6	-3365,3	$-5x10^{-4}$

Results

In the deformed mesh presented in Figure 5.26 it is visible that only translation between both parts of the model occurs. Figure 5.27 shows the resulting shear stress in the fracture. As expected, the fracture behaves elastically initially and when failure occurs it deforms at constant shear stress. It is also visible that the value for which the failure is reached changes for each confinement stress.

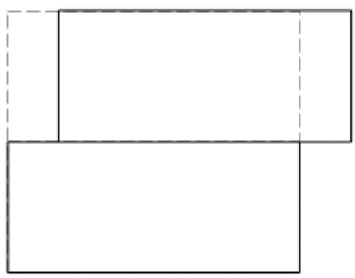

Figure 5.26 – Deformed mesh

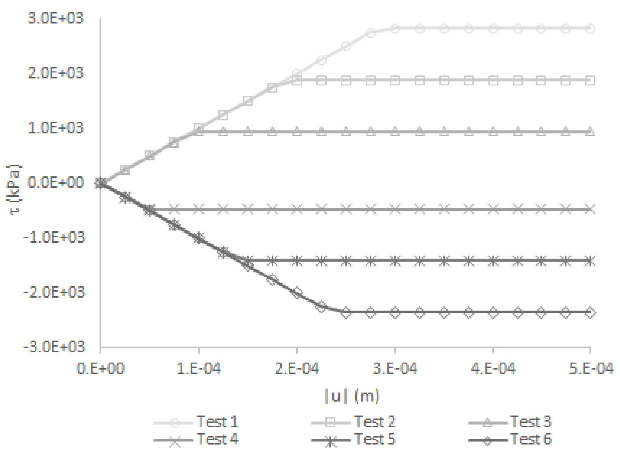

Figure 5.27 – Horizontal displacement versus shear stress in the fracture

In Figure 5.28, the normal and shear stresses in the fracture are plotted, so is the Mohr-Coulomb failure surface (in dashed lines). As only the shear stress varies during the simulations, the stress paths are vertical. It is evident that failure occurs at different shear values, depending on the normal stress, as stated by the Mohr-Coulomb constitutive law.

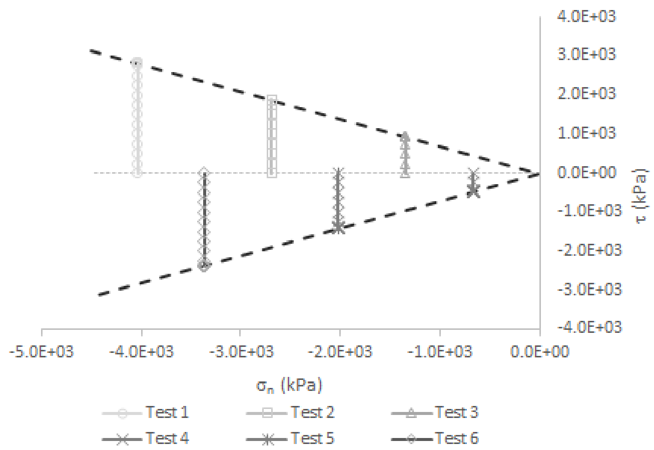

Figure 5.28 – Normal stress versus shear stress in the fracture

5.3.2. Single element with inclined fracture

<u>**General description of the simulation**</u>

As stated by several authors (Jiao and Qiao, 2008; Das, 2013; Esterhuizen, 2014), the results of a uniaxial compression test of a sample with a single fracture are strongly dependent on the fracture inclination. In order to simulate that effect, a model with a single element and one inclined fracture is subjected to uniaxial compression so the uniaxial strength is obtained for different fracture inclinations and compared with the analytical solution.

The analytical strength of a single fractured sample subjected to uniaxial stress may be obtained by the Mohr-Coulomb equation, as presented by Das (2013). The equation is given by

$$\sigma_1 = \frac{2.c}{(1 - \tan\varphi . \cot\beta)\sin 2\beta} \tag{5.2}$$

where c is the fracture cohesion, φ the friction angle and β the fracture angle with the horizontal. This solution is only valid for values of the inclination angle between φ and 90°, where it takes values of infinite. Therefore, it is assumed that the intact rock strength is 20 MPa so the fracture influences the results in a range between 36° and 84°. Moreover, the lowest strength is achieved for a fracture angle of $\pi/4 + \varphi/2$.

Model geometry and mesh

The model has a single rectangular element with dimensions 0,1 m x 0,01 m, as seen in Figure 5.29. A high height-width ratio is used in order to be sure that for all the tested inclinations the fracture crosses the element in the vertical boundaries. This way, different influence of the boundary conditions for different inclinations is avoided. Although it is widely known that such ratios are not recommended, it is considered that in this simple model it does not affect the results.

The fracture left extremity position is constant, while the right extremity changes with the fracture inclination. Seven different inclinations are tested: 37°, 40°, 50°, 60°, 70°, 80° and 83°.

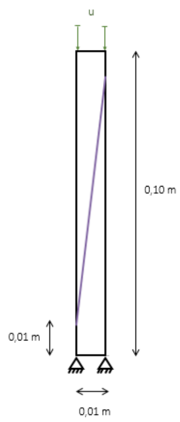

Figure 5.29 – Mesh and boundary conditions

<u>**Material properties**</u>

The mechanical properties of the solid region and the fracture are defined in Table 5.12. The fracture has a friction-cohesive behaviour given by the Mohr Coulomb model. A non-associated law is used, i.e. no dilatation occurs due to shear deformations.

Table 5.12 – Mechanical properties

	Parameter	Value
Solid Region	E (kPa)	$5x10^6$
	ν	0,25
Fracture	K_n (kPa)	0^{**}
	K_s (kPa)	10^8
	ϕ (°)	30
	c (kPa)	2000

**value in traction. In compression, a penalty factor is applied

<u>**Boundary and loading conditions**</u>

As seen in Figure 5.29, the model is fixed in its bottom and a prescribed displacement is applied at its top until failure occurs.

<u>**Results**</u>

Figure 5.30 shows that the obtained results match with the analytical solution. As expected, the fracture inclination affects the uniaxial strength in a range between 36° and 84°. As the inclination increases from 36°, the strength reduces reaching its bottom value at 60°, such as predicted by the Mohr-Coulomb model ($\pi/4 + \varphi/2 = 60°$). Figure 5.31 presents the fracture stress paths (normal and shear stresses) for the different inclinations. It is noticeable that failure occurs when the Mohr-Coulomb surface is reached and that the values of normal and shear stress at failure increase with a decrease of fracture inclination. This happens because lower inclinations imply higher normal stresses and consequently higher shear strength.

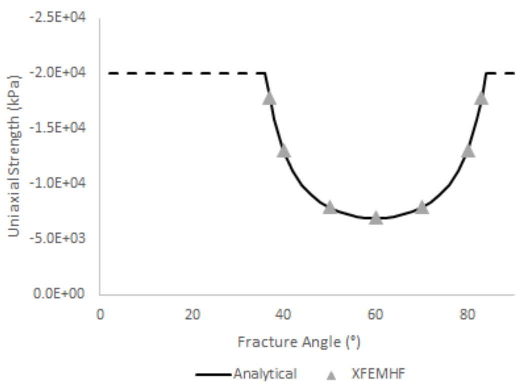

Figure 5.30 – Uniaxial strength variation with fracture inclination (assumed rock intact strength is plotted in dashed lines)

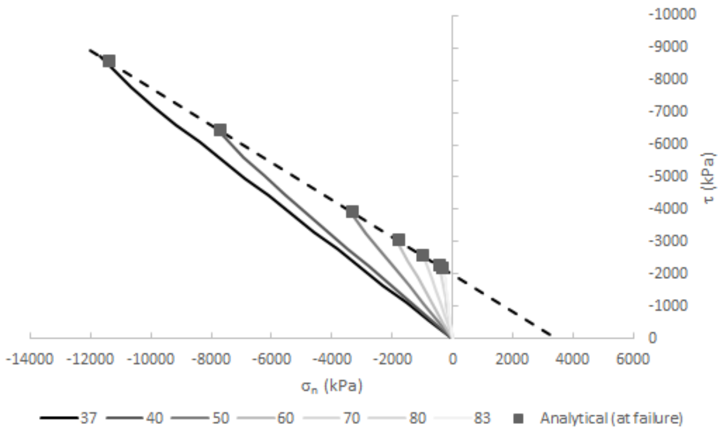

Figure 5.31 – Fracture stress paths for different fracture inclinations

5.3.3.
Multi-fractured medium

General description of the simulation

In this simulation, a sample with three intersecting fractures is subjected to a uniaxial compression at its top until failure is reached. As there is no analytical solution for this problem, the objective of this simulation is to assure that no fracture point crosses the failure surface defined by the Mohr-Coulomb model.

Model geometry and mesh

The model's dimensions are 15 m x 20 m and the mesh is regular with 15 and 20 elements in the horizontal and vertical directions, respectively, as seen in Figure

5.32. Three fractures are positioned in the sample in a way that two intersections occur.

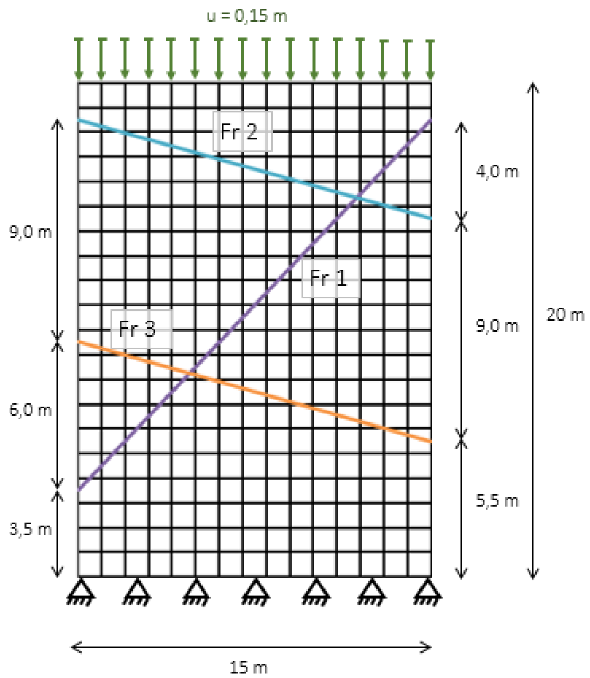

Figure 5.32 – Mesh and boundary conditions

Material properties

The mechanical properties of the solid region and the fractures are defined in Table 5.13. The fractures have a friction-cohesive behaviour given by the Mohr Coulomb model. A non-associated law is used, i.e. no dilatation occurs due to shear deformations.

Table 5.13 – Mechanical properties

	Parameter	Value
Solid Region	E (kPa)	10^6
	ν	0,3
Fractures	K_n (kPa)	0^{**}
	K_s (kPa)	10^5
	ϕ (°)	25
	c (kPa)	0

**value in traction. In compression, a penalty factor is applied

Boundary and loading conditions

As seen in Figure 5.32, the model is fixed in its bottom and a prescribed displacement of 0,15 m separated in 40 increments is applied at its top. Each increment size is defined by Abaqus automatic time incrementation algorithm, which reduces the increment size when convergence is harder to achieve and increases the increment size when few iterations are needed to converge.

Results

The simulation returned the expected behaviour of the model when subjected to the uniaxial load. In the deformed meshes at the end of two increments present in Figure 5.33 it is visible that relative movement between fracture faces occurred in every fracture.

Along the model there is no noticeable superposition of faces, except in the intersections (highlighted by grey dashed circumferences). This is an expected limitation of the model, as explained in Chapter 3.6.1.

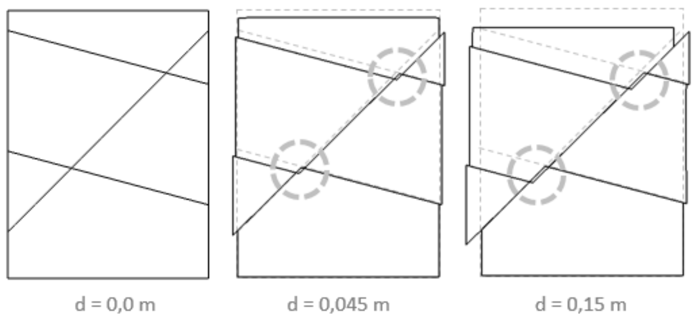

Figure 5.33 – Deformed mesh in different increments

Figure 5.34 shows the curve displacement-reaction at the top of the model. Although the Mohr-Coulomb model has an elastic-perfectly plastic constitutive behaviour, the whole model reacts with a stronger non-linearity due to the geometric position of the fractures.

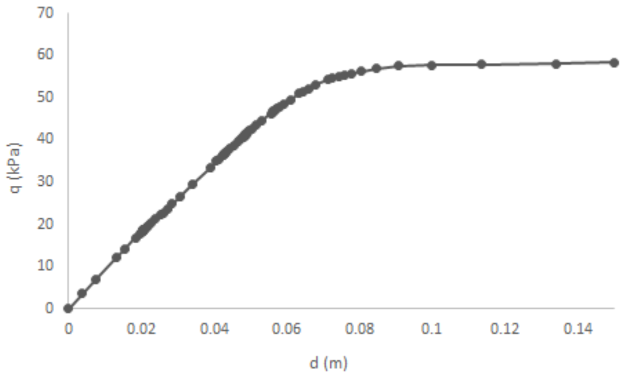

Figure 5.34 – Prescribed displacement vs reaction at the top of the model

Figure 5.35 presents the stress state in every fracture integration point of the model for each of the 3 fractures separately (see Figure 5.32 for each fracture number). Right after the first increment (Figure 5.35a), it is noticeable that even subjected to normal stress, all fractures are still in the elastic region. At an intermediate increment (Figure 5.35b), the shear stresses acting in the fractures increases. Shear stresses in fractures 1 and 2 take positive signs while fracture 3 has mostly negative values, as expected, due to each fracture inclination. It is also visible in Figure 5.35b that fracture 3 already has part of it in a failure situation. Finally, in the last increment of the simulation Figure 5.35c all the points in fracture 3 are in failure. Given that fracture 3 crosses the model from one side to the other, this corresponds to a generalized failure, as visible in Figure 5.34.

From the obtained results, it is noticeable that after reaching failure, deformation occurs at constant stress, so it may be concluded that all the fractures are modelling correctly the implemented contact-friction behaviour.

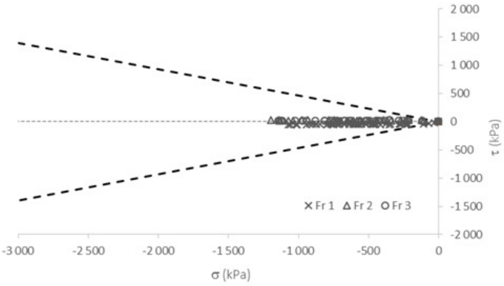

a)

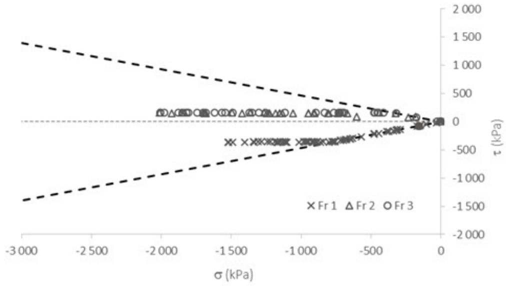

b)

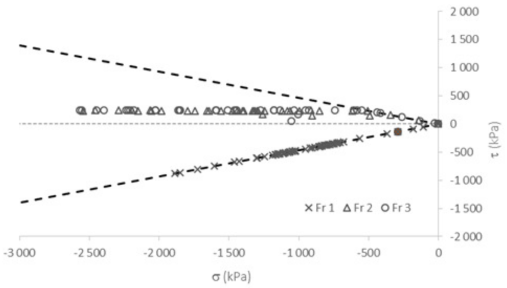

c)

Figure 5.35 – Fracture stress state (normal and shear stresses) for every fracture integration points of the model. a) d = 0,002 m. b) d = 0,045 m. c) d = 0,15 m.